Large Eddy Simulation of Non-Reactive Flow in a Pulse Detonation Chamber

IONUT PORUMBEL
Combustion Laboratory
Romanian National Research and Development Institute for Gas Turbines COMOTI
220D, Iuliu Maniu Blvd, 061126, Bucharest
ROMANIA
ionut.porumbel@comoti.ro http://www.comoti.ro

TUDOR CUCIUC
Institute for Applied Physics
Academy of Science
5, Academiei St, MD-2028, Chisinau
REPUBLIC OF MOLDOVA
cuciuctud@ phys.asm.md http://www.phys.asm.md

CLEOPATRA FLORENTINA CUCIUMITA
Turbines and Gas Turbines Assembly Department
Romanian National Research and Development Institute for Gas Turbines COMOTI
220D, Iuliu Maniu Blvd, 061126, Bucharest
ROMANIA
cleopatra.cuciumita@comoti.ro http://www.comoti.ro

CONSTANTIN EUSEBIU HRITCU
Combustion Laboratory
Romanian National Research and Development Institute for Gas Turbines COMOTI
9 – 11, Horia St, 700126, Iasi
ROMANIA
eusebiu.hritcu@comoti.ro http://www.comoti.ro

FLORIN GABRIEL FLOREAN
Combustion Laboratory
Romanian National Research and Development Institute for Gas Turbines COMOTI
220D, Iuliu Maniu Blvd, 061126, Bucharest
ROMANIA
florin.florean@comoti.ro http://www.comoti.ro

Abstract: - This is a sample of the format of your full paper. A You need to have A4-sized pages (21 x 29 cm) pages with top and bottom margins of 2.5 cm and left and right margins of 1.8 cm. Use single space. Use double- use column format after the Key-Words. Arrange the text in two columns (8.2 cm), each separated by a gap of 1 cm. Use 11 pt size Times New Roman throughout the paper except for the headlines. For the words *Abstract, Key-Words* and *References* Italics. Ensure that the text on the final page is spread so that both columns finish at the same distance from the top of the page.

Key-Words: - Leave one blank line after the Abstract and write your Key-Words (6 - 10 words)

1 Introduction

A pulsed combustor is a constant volume combustor operating under oscillatory conditions, based on the so-called Humphrey cycle [1], which is significantly more efficient than the constant pressure combustion, Brayton cycle, typical for the modern gas turbine engines [2]. If a detonation wave is used instead of a regular flame to burn the combustible

mixture, as in a Pulse Detonation Combustor (PDC), the speed of the burning process increases by several orders of magnitude and the thermal efficiency further increases [2,3]. A recent theoretical comparative study [2] of the efficiencies of the three cycles (constant pressure, constant volume, and detonation), indicates a thermodynamic efficiency of 27% for the Brayton cycle, of 47% for the Humphrey cycle, and of 49% for the detonation cycle. However, more recent research studies indicate that the superior efficiency of a pulsed detonation based cycle is only maintained up to flight Mach numbers of 3 [4]. Furthermore, NOx production is expected to be lower in a PDC, due to the significantly lower residence time and to the recirculation of the combustion products back into the combustion region [5].

If the detonation wave is assumed steady, planar, and one-dimensional, and if state 1 denotes the conditions for the reactants upstream of the detonation wave, while state 2 denotes the conditions for the products downstream of the detonation wave, then the Hugoniot relationship describing the energy release in a compressible flow is [6]:

$$\Delta h = h_2 - h_1 = \frac{1}{2}(p_2 - p_1)\left(\frac{1}{\rho_1} - \frac{1}{\rho_2}\right) \quad (1)$$

where h is the enthalpy, p is the pressure, and ρ is the density.

A graphical representation of Eq. (1) for a given initial state 1 with, and without (pure shock) energy release is presented in Fig. 1.

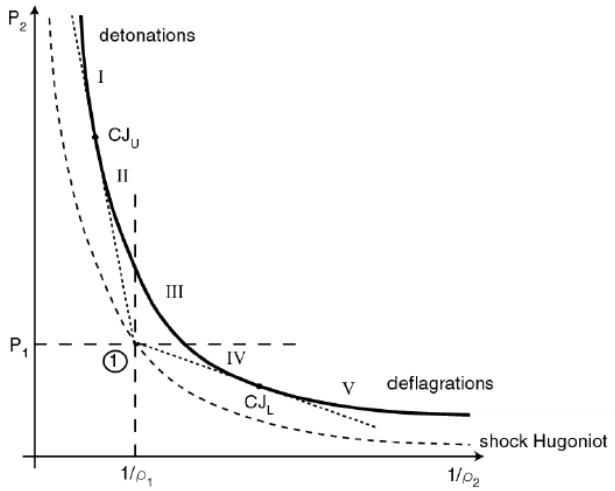

Fig. 1 - The Hugoniot curve without (dotted curve) and with energy release (solid curve)

The dotted lines 1 - CJ_L and 1 - CJ_U are the Rayleigh lines [6], tangent to the Hugoniot curve. The solutions located in regions I and II correspond to supersonic waves (detonations), while the solutions located in regions IV and V correspond to subsonic waves (deflagrations). Region I (strong detonations) can only be achieved if there is a piston forcing the compression behind the wave [6]. Region II (weak detonations) can only be found in extreme situations (eigenvalue solutions) [6]. Thermodynamically, point CJU represents the only readily achievable solution for detonation waves [6]. At point CJ_U, the flow behind the wave is sonic relatively to the wave ($M_2 = 1$). It can also be shown that the same point corresponds to a minimum entropy point [7], with positive implications on the combustion related entropy raise, which is the most significant contribution to the total entropy raise that determines the engine thermal efficiency [8]. The solutions in region III are not real [6]. Region IV (weak detonations) corresponds to laminar flames. Region V (strong deflagrations), cannot be achieved in a constant area duct [9]. For deflagrations, the propagation speed is a function of the combustion wave structure of and of the turbulent and diffusive transport properties. For detonations, the propagation speed is determined by gas dynamic considerations. A point similar to CJU, CJL, exists on the lower, deflagration, branch, but, as the entire region IV is acceptable thermodynamically, this point does not represent a special case.

The planar detonation wave is periodically initiated at one end of the combustor and travels at the Chapman - Jouguet velocity [6] towards the opposite end. After the detonation wave leaves the chamber, a set of expansion waves forms, decreasing the pressure and evacuating the combustion products.

2 The Pulse Detonation Chamber

2.1 PDC constructive definition

The paper presents the non-reactive numerical simulations carried out for the PDC presented in Fig. 2.

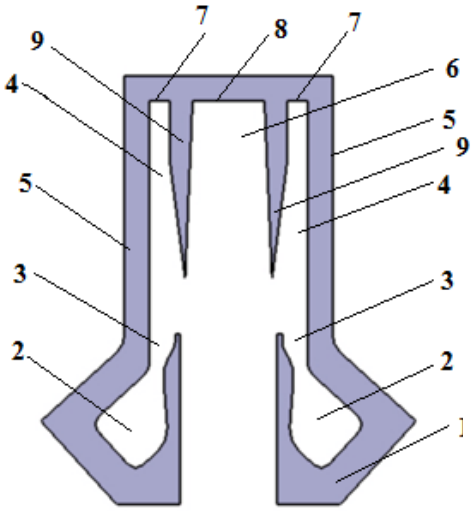

Fig. 2 – PDC geometry

The combustor is of rectangular construction, will include shockwave generator with coupled resonators and consists of the following:

1. Combustor casing;
2. High pressure air chambers;
3. Supersonic nozzle;
4. Lateral resonators;
5. Outer side walls of the lateral resonators;
6. Central detonation chamber;
7. End walls of the lateral resonators;
8. End wall of the central resonator;
9. Separation walls.

The combustor (1) is fed by the high pressure air chambers (2), where the air is delivered by the engine compressors and which feed the air into the supersonic nozzles (3). Two lateral resonators (4), delimited by walls (5), (7) and (9) are placed with their open endings towards the supersonic nozzles (3). Between the lateral resonators (4), the central detonation chamber (6) is placed, delimited by walls (8) and (9). The central detonation chamber (6) and the two lateral resonators (4) are separated by sharp angled walls (9), with the sharp angle edge placed at the open end of the central detonation chamber (6).

2.2 PDC aerodynamics

The PDC's operation is based on supersonic jets, formed by the diverging end supersonic nozzles (3). The use of supersonic jets is expected to provide an increase in temperature at the closed ends of the resonators (4) and of the central detonation chamber (6), as compared to the sonic jets [10], due to the increase in velocity at the nozzles exit.

As the supersonic jets impact the sharp edged walls (9) placed at the open ends of the lateral resonators (4), shock waves are formed and travel towards the closed end of the resonators (7). The air stream including the air in the supersonic stream in the region behind the Mach disk and the air in the lateral and central regions entrained by the supersonic jets shear layers is directed into the lateral resonator chambers (4). The air stream detaches in the central region of the combustor from the side walls (5) and enters the lateral resonators (5) at a variable angle with respect to the combustor centreline. The travelling shock waves impact the end walls of the resonators (7) and are reflected backwards, towards the lateral resonators (4) open ends, causing an increase in the wall pressure. An earlier model of the proposed resonator tubes and their operation can be found in [11, 12].

When the backwards travelling shockwaves reach the open ends of the lateral resonators (4), they are converted into expansion waves. This moment in time separates the two operation phases of the resonator: the filling phase, before the previously mentioned point in time, and the exhaust phase, which follows.

During the filling phase, the air stream velocity in the lateral resonators (4) decreases to zero, and the air mass flow rate deflected around the lateral resonators (4) into the central detonation chamber (6) continuously increases up to the maximum value, which is the inlet mass flow rate. During this process, the velocity of the supersonic jets is basically constant.

The filling phase can be further divided into two sub-phases. In the first, the air mass flow rate entering the central detonation chamber (6) increases slowly, as the velocity of the air stream entering the lateral resonators (4) decreases from the maximum value to zero. In the second sub-phase, both the air mass flow rate entering the central detonation chamber, and its velocity suffer a jump increase due to the sudden opening of the transversal cross-section between the supersonic jets and the side walls (5), allowing the evacuation of the air from the lateral resonators (4). The second sub-phase is significantly shorter than the first sub-phase, creating the conditions for a shock wave to appear in the central detonation region (6), travelling towards its closed end (8). If the proper conditions for creating such a shock wave are not met, then a sonic pressure wave with a ¼ wavelength is formed inside the central detonation chamber (6). In this case, a supplementary increase in the pressure at the central detonation chamber end wall (8) can be achieved through proper profiling of the central detonation chamber [13].

During the exhaust phase, the air from the lateral resonators (4) is exhausted initially due to the pressure difference between the lateral resonators

(4) and the central detonation chamber (6), and through supersonic jet entrainment afterwards. This process is very fast and it ends up by creating a maximum pressure deficit inside the lateral resonators (4). At the end of the exhaust phase, the supersonic jets outside the lateral resonators (4) is directed towards the combustor exit, forming two planar high speed jets, as if separated by a central body. At this point, he pressure on the on the central detonation chamber end wall (8) is maximum.

As a new filling phase starts, the supersonic jet is suddenly deviated towards the lateral resonator wall (5). In the same time, part of the fluid in the central detonation chamber (6) is injected into the lateral resonators (4), under the initial action of the pressure difference, and by jet entrainment afterwards. The deviation of the supersonic jet towards the lateral wall opens up the way for the evacuation of the fluid in the central detonation chamber (6) through the combustor outlet.

The cycle of successively generating shock waves through the impact of the supersonic jet with the lateral resonators (4) and the central combustion chamber (6) has a frequency that is a function of the local speed of sound and of the length of the lateral resonators (4) and central detonation chamber (6), chosen to be of equal length. This effectiveness of this choice has to be confirmed through CFD studies at a later stage.

The advantage of the presented constructive solution resides in converting a larger fraction of the supersonic jets kinetic energy to shock wave energy by using the exhaust phase supersonic jet kinetic energy as well. In conventional Hartman generators, this supersonic jet kinetic energy is not used, and is exhausted by the resonator fluid in the ambient air.

The sharp edges of the walls (9) are used in order to reduce the aerodynamic drag imposed on the exhaust jet. Also, an increase in the shock wave amplitude is expected due to the superposition of the oblique shockwave reflected backwards by the central detonation chamber end wall (8), over the normal shock wave.

The shape of the diverging channel of the supersonic nozzles (3) was designed to ensure a faster deviation of the supersonic jet towards the lateral wall during the shock wave formation phase.

3 Numerical Setup

3.1 LES Algorithm

The numerical results presented herein were obtained by using a Large Eddy Simulation (LES) of the non-reactive flow through the PDC presented in the previous section. The LES algorithm employed for the numerical simulations was developed at COMOTI [14] and is a second order in space and first order in time accurate fully compressible algorithm based on a 5 step modified Runge - Kutta numerical scheme, employing a Localized Dynamic Turbulent Kinetic Energy turbulence model.

The earliest application of the Large Eddy Simulation (LES) methodology was performed by Smagorinsky [15] and important further developments of the method were introduced later [16, 17, 18, 19].

LES resolves both the large, geometry dependent turbulent scales and a fraction of the smaller energy containing scales within the inertial range, up to a level dictated by the resolution of the numerical grid, and only the remaining scales are modeled. If the grid resolution is appropriately chosen, the unresolved scales, by Kolmogorov's hypothesis [20] are isotropic and, therefore, more amenable to modeling. This approach not only provides a lot more information but since the energy contained in the unresolved scales is much less than in the RANS approach, is also less sensitive to modeling hypotheses.

The separation between the large (resolved) and the small (modeled) scales is determined by the grid size Δ.

The fully compressible Navier-Stokes equations describing the conservation of mass, momentum, and total energy in non – reacting flow are:

$$\begin{cases} \frac{\partial \rho}{\partial t} + \frac{\partial \rho u_i}{\partial x_i} = 0 \\ \frac{\partial \rho u_i}{\partial t} + \frac{\partial}{\partial x_j}\left(\rho u_i u_j + p\delta_{ij} - \tau_{ij}\right) = 0 \\ \frac{\partial \rho E}{\partial t} + \frac{\partial}{\partial x_i}\left[(\rho E + p)u_i + q_i - u_j \tau_{ij}\right] = 0 \end{cases} \quad (2)$$

In the above equations, u_i is the i-th velocity component, ρ is the mass density, p is the pressure, E is the total energy per unit mass, written as [14]:

$$E = e + \frac{1}{2}(u_k u_k) \quad (3)$$

and τ_{ij} is the viscous stress tensor, defined as:

$$\tau_{ij} = \mu\left(\frac{\partial u_i}{\partial x_j} + \frac{\partial u_j}{\partial x_i}\right) - \frac{2}{3}\frac{\partial u_k}{\partial x_k}\delta_{ij} \quad (4)$$

where δ_{ij} is the Kronecker delta function.

Also, e is the internal energy per unit mass computed as [14]:

$$e = h - \frac{p}{\rho} \quad (5)$$

where h is the enthalpy per unit mass:

The heat flux vector in Eq. (2) can be expressed as (neglecting radiation) [14]:

(6)

$$q_i = -\kappa \frac{\partial T}{\partial x_i}$$

where T is the temperature and κ is the thermal conductivity.

The pressure p is directly derived from the equation of state for perfect gas, where R is he gas constant [14]:

$$p = \rho R T \tag{7}$$

The viscosity is determined using Sutherland's law:

$$\frac{\mu}{\mu_0} = \frac{\left(\frac{T}{T_0}\right)^{3/2}}{\frac{T_s+T}{T_0}} \tag{8}$$

where μ_0 is the reference viscosity at temperature T_0 and T_s = 110,4 K.

The Navier-Stokes equations (2) have to be filtered with respect to the grid size in order to obtain the LES governing equations. A Favre spatial top-hat filter is employed to derive the LES equations. More details regarding the LES filtering and the different techniques are given elsewhere [21, 22].

By applying the above mentioned filtering process to Eq. (2), the LES filtered Navier-Stokes equations can be written as [23]:

$$\begin{cases} \dfrac{\partial \overline{\rho}}{\partial t} + \dfrac{\partial \overline{\rho}\widetilde{u_\iota}}{\partial x_i} = 0 \\ \dfrac{\partial \overline{\rho}\widetilde{u_\iota}}{\partial t} + \dfrac{\partial}{\partial x_j}\left(\overline{\rho}\widetilde{u_\iota}\widetilde{u_J} + \overline{p}\delta_{ij} - \overline{\tau_{ij}} + \tau_{ij}^{sgs}\right) = 0 \\ \dfrac{\partial \overline{\rho}\tilde{E}}{\partial t} + \dfrac{\partial}{\partial x_i}\left[\left(\overline{\rho}\tilde{E} + \overline{p}\right)\widetilde{u_\iota} + \overline{q_i} - u_j\overline{\tau_{ij}} + H_i^{sgs} + \sigma_i^{sgs}\right] = 0 \end{cases} \tag{9}$$

In the above, the over-bar denotes the spatial filtering and the ~ symbol denotes the Favre filtering.

If, in the following, k^{sgs} is the sub-grid turbulent kinetic energy, defined as [14]:

$$k^{sgs} = \frac{1}{2}\left(\widetilde{u_k u_k} - \widetilde{u_k}\widetilde{u_k}\right) \tag{10}$$

the LES filtered total energy per unit mass can be written as [14]:

$$\tilde{E} = \tilde{e} + \frac{1}{2}\left(\widetilde{u_k}\widetilde{u_k}\right) + k^{sgs} \tag{11}$$

The LES filtered viscous stress tensor and the filtered heat flux can be written by using filtered quantities in Eq. (4) and respectively Eq. (6). The equation of state (7) can also be written using filtered quantities.

The LES filtered equations (9) contain unresolved terms representing the effects of the unresolved scales on the resolved motion, resulting from the filtering process and denoted by the superscript sgs.

These unclosed terms that need to be modeled are: the sub-grid kinetic energy, k^{sgs}, the shear stress tensor, τ_{ij}^{sgs}, the sub-grid enthalpy flux, H_i^{sgs} and the sub-grid viscous work, σ_i^{sgs}.

The turbulence model, used to close the unresolved terms mentioned earlier, is a non - equilibrium model based on the sub-grid kinetic energy transport equation, initially developed by Schumann [24] and later improved by other researchers [25, 26, 27]. The model assumes isotropic turbulence at the sub-grid scales and tracks the sub-grid kinetic energy, k^{sgs}, using a formally derived transport equation, equation solved along with the rest of the LES equations:

$$\begin{aligned} \frac{\partial \overline{\rho} k^{sgs}}{\partial t} + \underbrace{\frac{\partial}{\partial x_i}\left(\overline{\rho}\widetilde{u_\iota}k^{sgs}\right)}_{I} = &\underbrace{-\frac{\partial}{\partial x_i}\left(\widetilde{\rho k u_\iota} - \overline{\rho}\tilde{k}\widetilde{u_\iota}\right)}_{II} \\ &\underbrace{-\left(\widetilde{u_\iota\frac{\partial p}{\partial x_\iota}} - \widetilde{u_\iota}\frac{\partial \overline{p}}{\partial x_i}\right)}_{III} \underbrace{-\left(\widetilde{u_\iota\frac{\partial \tau_{\iota J}}{\partial x_\iota}} - \widetilde{u_\iota}\frac{\partial \overline{\tau_{ij}}}{\partial x_i}\right)}_{IV} \\ &\underbrace{-\frac{\partial}{\partial x_i}\left(\widetilde{u_J}\tau_{ij}^{sgs}\right)}_{V} \underbrace{-\tau_{ij}^{sgs}\frac{\partial \widetilde{u_J}}{\partial x_i}}_{VI} \end{aligned} \tag{12}$$

where:

$$k = \frac{1}{2}\left(\widetilde{u_k}\widetilde{u_k}\right) \tag{13}$$

In Eq. 12, term (I) represents the resolved convection, terms (II) and (III) the sub-grid turbulent convection, term (IV) is the sum of the sub-grid stress work and the turbulent kinetic energy dissipation, term (V) represents the sub-grid transport of turbulent kinetic energy and (VI) the turbulent kinetic energy production. Terms (II) to (VI) require closure.

The three sub-grid turbulent convection terms (II), (III) and the sub-grid stress work (IV_1) are modeled together as:

$$II + III + IV_1 = -\frac{\partial}{\partial x_i}\left[\overline{\rho}\frac{(\nu+\nu_t)}{\sigma_k}\frac{\partial k^{sgs}}{\partial x_i}\right] \tag{14}$$

Here, σ_k is a constant assumed to be unity [28].

The production of sub-grid turbulent kinetic energy (P^{sgs}) can be expressed in terms of the sub-grid stress tensor:

$$P^{sgs} = -\tau_{ij}^{sgs}\frac{\partial \widetilde{u_\iota}}{\partial x_j} \tag{15}$$

Finally, the dissipation of sub-grid turbulent kinetic energy (D^{sgs}) is modeled as:

$$D^{sgs} = C_\epsilon \frac{\sqrt{(k^{sgs})^3}}{\overline{\Delta}} \tag{16}$$

Once the sub-grid kinetic energy is known from solving Eq. 12, the sub-grid length scale is given by the filter size, Δ, the velocity scale, V^{sgs} is determined from k^{sgs} and the eddy viscosity is modeled as:

$$\upsilon_t = C_\upsilon \sqrt{k^{sgs}}\,\overline{\Delta} \tag{17}$$

The sub-grid stress tensor τ_{ij}^{sgs}, is then closed using the sub-grid eddy viscosity and a gradient diffusion model at the grid cutoff scale:

$$\tau_{ij}^{sgs} = -2\bar{\rho}\nu_t\left(\widetilde{S_{\iota J}} - \frac{1}{3}\widetilde{S_{kk}}\delta_{ij}\right) + \frac{2}{3}\overline{\rho}k^{sgs}\delta_{ij} \tag{18}$$

where the resolved strain rate is defined as:

$$\widetilde{S_{\iota J}} = \frac{1}{2}\left(\frac{\partial \widetilde{u_\iota}}{\partial x_j} + \frac{\partial \widetilde{u_J}}{\partial x_i}\right) \tag{19}$$

It is important to note that even though the sub-grid stress tensor model employs a gradient diffusion assumption, the large scale counter-gradient effects are accounted for, since the large scales are resolved.

The sub-grid enthalpy flux H_i^{sgs}, is also modeled using a gradient assumption and the eddy viscosity given by Eq. 17:

$$H_i^{sgs} = -\overline{\rho}\frac{\nu_t}{Pr_t}\frac{\partial \widetilde{H}}{\partial x_i} \quad (20)$$

where Pr_t is the turbulent Prandtl number, and the total enthalpy is given by:

$$\widetilde{H} = \tilde{h} + \frac{\widetilde{u_i}\widetilde{u_i}}{2} + k^{sgs} \quad (21)$$

where $\tilde{h}$ is the specific mixture enthalpy.

The turbulent Prandtl number is assumed in this study as unity, following earlier studies [14, 23]. The sub-grid work, σ_i^{sgs}, is neglected here, as in earlier studies [14, 23].

In the previous equations there are two model coefficients C_ε in Eq. 16 and Cν in Eq. 17 that are obtained dynamically as a part of the solution, using a method called the "Localized Dynamic Kinetic energy Model" (LDKM) [29, 30].

The LDKM model assumes that the resolved and the unresolved small scales behave in a similar manner and, thus, the model coefficients can be computed using similarity relationships. First, a test-filter, operating in a region close to the cutoff scale, at the small, but still resolved, scales is defined. Usually, the size of the test-filter is twice the LES resolution. Since the turbulent quantities are known at the test-filter level, the LES model coefficients can be determined by comparing quantities resolved at the two filter scales. For details on the LDKM model, see the cited work and also reference [23].

LDKM is locally stable in both space and time without smoothing. and its advantage consists in the fact that no spatial averages are required, which makes the model easy to implement in complex geometries. Past studies [31, 32], and commercial code evaluations [33] has demonstrated the reliability and accuracy of the LDKM closure.

3.2 Computational Grid

The computational domain has been divided into 13 blocks, in order to allow the proper setting of the boundary conditions on the computational domain. The 13 blocks are presented in Figure 3, together with the coordinate system used for the discretization of the computational domain. The origin of the coordinate system is placed on the symmetry axis of the combustor, in the exhaust section, and at the middle of the spanwise dimension z. The 13 domains presented in Figure 3 extend over the entire computational domain along the z axis.

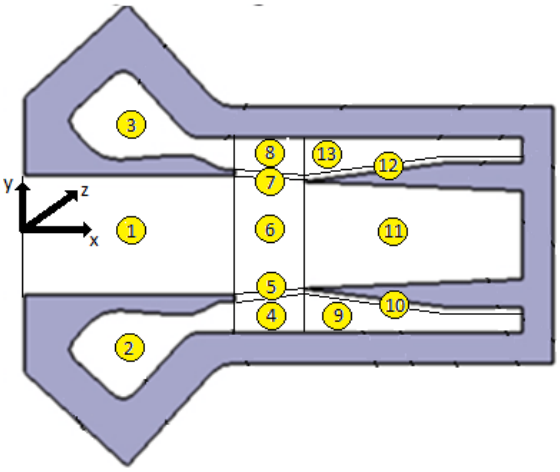

Fig. 3 – Definition of the discretization blocks

The computational discretization grid was defined for each block such that the computational cells at the edges of each block to match the computational cells of its adjacent blocks on every spatial direction.

The difference in size on any spatial direction between any two adjacent cells must not exceed 10 % (preferably 5 %).

The computational cells were clustered towards the walls and towards the regions of increased interest for the computation (such as regions where shock waves and detonation waves are expected. The total number of grid cells is of 2,180,546.

The integral length scale [1] of the flow through the combustor is of the order of the combustor length, *L = 80 mm*. The typical Reynolds number of the flow is given by [22]:

$$\mathrm{Re} = \frac{\rho \mathrm{U} \mathrm{L}}{\mu} \quad (22)$$

The flow Mach number varies significantly in the flow, both in space, and in time, depending on the moment in the detonation cycle. However, it can be estimated that a characteristic Mach number for the flow must reside between the inlet Mach number $\mathrm{M_{in}} = 0.62$ and the Mach number before detonation $\mathrm{M_{det}} = 1.83$. Thus, the characteristic flow Mach number can be considered to be $\mathrm{M} = 1.225$.

Similarly, the temperature varies between the inlet temperature $\mathrm{T_{in}} = 500\ \mathrm{K}$ and the adiabatic flame temperature for propane or acetylene $\mathrm{T_{ad}} = 2700 - 2800\ \mathrm{K}$. Thus, the characteristic flow temperature can be considered to be $\mathrm{T} = 1625\ \mathrm{K}$.

Since the velocity can be expressed as [22]:

$$\mathrm{U} = \mathrm{Ma} \quad (23)$$

and the speed of sound in air corresponding to temperature T is [22]:

$$\mathrm{a} = \sqrt{\mathrm{kRT}} \quad (24)$$

Hence, the characteristic speed of sound in the flow is: $a = 802.4\ m/s$ and the characteristic velocity of the flow can be considered as $U = 982.9\ m/s$.
As for temperature and Mach number, the pressure in the combustor flow is expected to vary between the atmospheric exhaust pressure and the pressure after detonation. However, the detonation pressure only occurs for a very short time, and in a limited region of the combustor. Hence, the mean flow pressure will be selected as the inlet pressure $p_{in} = 6\ bar$. Therefore, the mean flow density can be expressed from the state equation for air (7), as $\rho = 1.3\ kg/m^3$. Then, the characteristic temperature given by (8), the air viscosity is $\mu = 5.63 \cdot 10^{-5}\ {}^{kg}/_{ms}$Thus, the mean flow Reynolds number is found to be $Re = 1.8 \cdot 10^6$. The Kolmogorov length scale of the flow is, then [22]:

$$\eta = L \cdot Re^{-3/4} \qquad (25)$$

or: $\eta = 1.6 \cdot 10^{-6} m$. To achieve LES resolution, the discretization grid was built to have cell sizes in the range:

$$\Delta \in (60 - 600)\eta \qquad (26)$$

Considering all these, the number of grid points selected in each block is given in Table 1.

Table 1– Discretization grid and computational grid sizes.

Block	i	j	k
1	Number of cells		
	123	78	44
	Cell size		
	1.000x10^{-4} - 9.908x10^{-4}	1.575x10^{-4} - 2.988x10^{-4}	1x10^{-3}
2	Number of cells		
	177	25	44
	Cell size		
	1.000x10^{-4} - 4.997x10^{-4}	1.000x10^{-4} - 5.200x10^{-4}	1x10^{-3}
3	Number of cells		
	177	25	44
	Cell size		
	1.000x10^{-4} - 4.997x10^{-4}	1.000x10^{-4} - 5.200x10^{-4}	1x10^{-3}
4	Number of cells		
	110	25	44
	Cell size		
	1.000x10^{-4}	1.600x10^{-4} - 2.400x10^{-4}	1x10^{-3}
5	Number of cells		
	110	6	44
	Cell size		
	1.000x10^{-4}	1.657x10^{-4} - 1.680x10^{-4}	1x10^{-3}
6	Number of cells		
	110	78	44
	Cell size		
	1.000x10^{-4}	1.240x10^{-4} - 2.988x10^{-4}	1x10^{-3}
7	Number of cells		
	110	6	44
	Cell size		
	1.000x10^{-4}	1.657x10^{-4} - 1.680x10^{-4}	1x10^{-3}
8	Number of cells		
	110	25	44
	Cell size		
	1.000x10^{-4}	1.600x10^{-4} - 2.400x10^{-4}	1x10^{-3}
9	Number of cells		
	113	25	44
	Cell size		
	9.970x10^{-5} - 4.999 x10^{-4}	1.200x10^{-4} - 2.400x10^{-4}	1x10^{-3}
10	Number of cells		
	113	6	44
	Cell size		
	9.970x10^{-5} - 4.999 x10^{-4}	1.657x10^{-4} - 1.680x10^{-4}	1x10^{-3}
11	Number of cells		
	113	6	44
	Cell size		
	9.970x10^{-5} - 4.999 x10^{-4}	1.000x10^{-4} - 2.825x10^{-4}	1x10^{-3}
12	Number of cells		
	113	6	44
	Cell size		
	9.970x10^{-5} - 4.999 x10^{-4}	1.657x10^{-4} - 1.680x10^{-4}	1x10^{-3}
13	Number of cells		
	113	25	44
	Cell size		
	9.970x10^{-5} - 4.999 x10^{-4}	1.200x10^{-4} - 2.400x10^{-4}	1x10^{-3}

A summary of the boundary conditions imposed in the numerical simulation for each block is given in Table 2:

Table 2– Boundary conditions.

Block	Direction i		Direction j		Direction k	
	min	max	min	max	min	max
1	E	6	W	W	W	W
2	I-W	4	W	W	W	W
3	I-W	8	W	W	W	W
4	2	9	W	5	W	W
5	W	10	4	6	W	W
6	1	11	5	7	W	W
7	W	12	6	8	W	W
8	3	13	7	W	W	W
9	4	W	W	10	W	W
10	5	W	9	W	W	W
11	6	W	W	W	W	W
12	7	W	W	13	W	W
13	8	W	12	W	W	W

In the above table, the numbers represent the adjacent blocks, *E* represents extrapolation boundary conditions, I-W represent mixed subsonic characteristic inflow and solid, no-slip, adiabatic wall boundary conditions, and W represent solid, no-slip, adiabatic wall boundary conditions. All these boundary conditions are described elsewhere [14].

4 Results and Discussion

The instantaneous Mach number field in the unlit PDC is presented in Fig. 4.

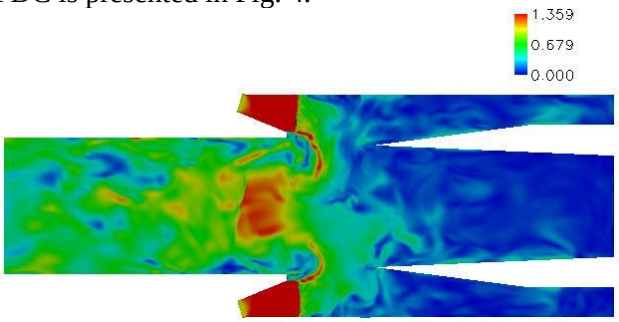

Fig. 4 – Instantaneous Mach number field

As expected, the air accelerates to supersonic velocities in the divergent nozzle downstream of the critical section, and a shock wave is formed at the end of the nozzle (Fig. 5), due to the sudden expansion.

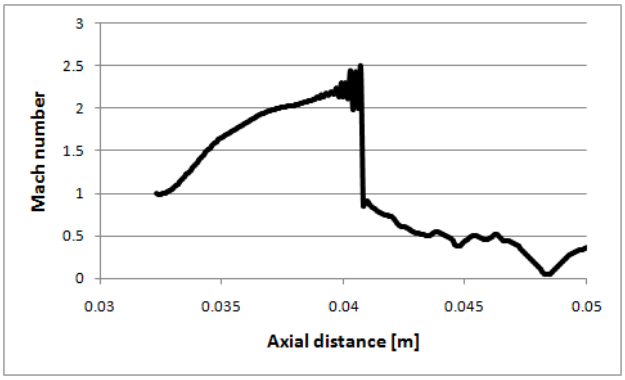

Fig. 5 – Instantaneous Mach number along the inlet nozzle axis

The high pressure created at the end wall forces the air stream to reverse its flow direction towards the outflow, and a new supersonic region occurs in the central region of the PDC. The flow direction can be better appraised in Fig. 6.

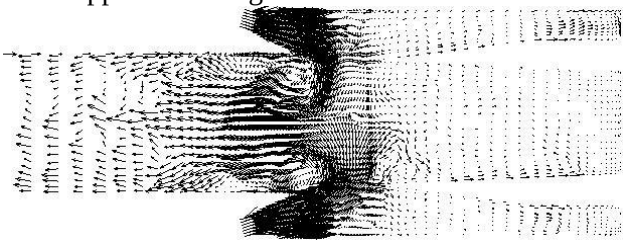

Fig. 6 – Instantaneous velocity vector field

Since no heat is added through combustion, the energy in the flow is insufficient to sustain the supersonic flow, and the air velocity decreases to subsonic values at the PDC outlet, as shown in Fig. 7.

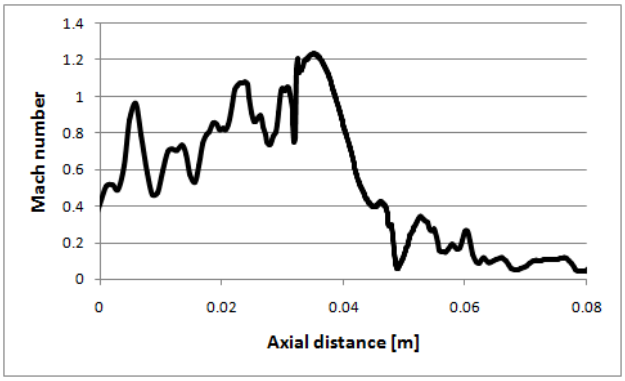

Fig. 7 – Instantaneous Mach number along the PDC axis

One of the main reasons for carrying out the PDC non-reactive flow simulation was to analyze the correlation between the pressure waves travelling in the main combustion chamber and in the resonators. Thus, Fig. 8 presents the time variation of the instantaneous pressure on the main combustion chamber centerline at three axial locations, while Fig. 9 presents the time variation of the instantaneous pressure on the resonator centerline at the same axial locations. The axial distance is

measured downstream from the separation walls sharp edges.

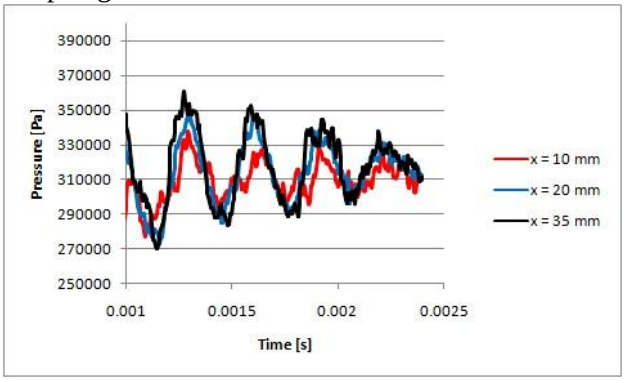

Fig. 8 – Time variation of the instantaneous pressure at three axial locations on the main combustion chamber axis

The pressure waves that are formed at the exit of the supersonic nozzles travel in the two resonators, as well as in the main combustion chamber, as shown in Fig. 8.

5 Conclusion

Please, follow our instructions faithfully, otherwise you have to resubmit your full paper. This will enable us to maintain uniformity in the conference proceedings as well as in the post-conference luxurious books by WSEAS Press. Thank you for your cooperation and contribution. We are looking forward to seeing you at the Conference.

References:

[1] C.E. Hriţcu, *Research on Pulsed Operation Combustion Chambers*, Ph.D. Thesis, "Gh. Asachi" Technical University, Iaşi, 2004

[2] K. Kailasanath, Review of Propulsion Applications of Detonation Waves, AIAA Journal, Vol.38, No.9, 2000

[3] E. Wintenberger, J.E. Shepherd, Thermodynamic Cycle Analysis for Propagating Detonations, Journal of Propulsion and Power, Vol.22, No.3, pp. 694 - 697, 2006

[4] W.H. Heiser, D.T. Pratt, Thermodynamic Cycle Analysis of Pulse Detonating Engines, Journal of Propulsion and Power, Vol.18, No.1, pp. 68 - 76, 2002

[5] G. Plavnik, Pulse Combustion Technology, 14th North American Waste to Energy Conference, NAWTEC14-3195, Tampa, Florida, USA, 2006

[6] S.R. Turns, *An Introduction to Combustion*, McGraw - Hill, London, 2000

[7] D.L. Chapman, On the Rate of Explosions in Gases, Philosophy Magazine, Vol.47, pp. 90 - 104, 1899

[8] E. Wintenberger, *Applications of Steady and Unsteady Detonation Waves to Propulsion*, Ph.D. Thesis, California Institute of Technology, Pasadena, CA, 2004

[9] J.D. Anderson, *Modern Compressible Flows*, McGraw-Hill, Second Edition, 1990

[10] V.V. Semenov, L. Min, I.E. Ivanov, I.A. Kryukov, Gas-Dynamic Igniter with Supersonic Nozzle, Vestnik Moskovskogo Aviatsionnogo Instituta Journal, Vol.11, No.2, pp.22-27, 2004

[11] J. Danton, F. Villas Boas, K.V. Kessaev, M. Niwa, Some Peculiarities if the Resonance Tube Gas-Dynamical Heating, ENCIT 2000, Brazilian Congress of Thermal Engineering and Sciences, 2000

[12] K.V. Kessaev, Theoretical Model of Resonance Tube, Aviationnaja Technica, pp. 49-52, 1990

[13] W.A. Denne, Pulse Jet Engines, US Patent US20080209884 A1, 2008

[14] I. Porumbel, C. Cârlănescu, F.G. Florean, C.E. Hriţcu, LES Algorithm for Turbulent Reactive Flows Simulation, Applied Computing Conference, Timişoara, Romania, 2010

[15] J. Smagorinsky, General Circulation Experiments with the Primitive Equations. I. The Basic Experiment, Monthly Weather Review, Vol.91, No.3, pp. 99 - 164, 1963.

[16] M. Germano, P. Piomelli, U. Moin, W. H. Cabot, A Dynamic Sub-Grid Scale Eddy Viscosity Model, Proceedings of the Summer Program, pp 5-17, 1990.

[17] P. Moin, W. Squires, W. Cabot, S. Lee, A Dynamic Sub-Grid Scale Model for Compressible Turbulence and Scalar Transport, Journal of Fluid Mechanics, Vol. 3, No. 11, 1991, pp. 2746-2757.

[18] G. Erlebacher, M.Y. Hussaini, C.G. Speziale, T.A. Zang, Toward the Large Eddy Simulation of Compressible Turbulent Flows, Journal of Fluid Mechanics, Vol. 238, 1992, pp. 155-185.

[19] S. Menon, Active Combustion Control in a Ramjet using Large Eddy Simulations. Combustion Science and Technology, Vol. 84, 1992, pp. 51-79.

[20] A.N. Kolmogorov, Local Structure of Turbulence in Incompressible Fluids with Very High Reynolds Number. Dokl. Acad. Nauk, Vol. 30, 1941, pp. 229.

[21] S. Ghosal, *On the Large-Eddy Simulation of Turbulent Flows in Complex Geometries*, Technical report, Center for Turbulence Research, 1993.

[22] S.B. Pope, *Turbulent Flows*, Cambridge University Press, 2000.

[23] I. Porumbel, *LES of Bluff Body Stabilized Premixed and Partially Premixed Combustion*, VDM Verlag Dr. Muller, Saarbrücken Germany, 2006
[24] U. Schumann, Subgrid Scale Model for Finite Difference Simulations of Turbulent Flows in Plane Channels and Annuli, Journal of Computational Physics, Vol. 18, 1975, pp. 376-404
[25] W.W. Kim, S. Menon, A New Incompressible Solver for Large - Eddy Simulations, International Journal of Numerical Methods in Fluids, Vol. 31, 1999, pp. 983-1017.
[26] W.W. Kim, S. Menon, H.C. Mongia. Large Eddy Simulation of a Gas Turbine Combustor Flow, Combustion Science and Technology, Vol. 143, 1999, pp. 25-62.
[27] S. Menon, P.K. Yeung, W.W. Kim, Effect of Subgrid Models on the Computed Interscale Energy Transfer in Isotropic Turbulence, Computers and Fluids, Vol. 25, No. 2, 1996, pp. 165-180.
[28] C. Fureby, *On Modeling of Unsteady Combustion Utilizing Continuum Mechanical Mixture Theories and Large Eddy Simulations*, PhD thesis, Lund Institute of Technology, Lund, Sweden, 1995.
[29] W.W. Kim, S. Menon, A New Dynamic One-Equation Subgrid-Scale Model for Large-Eddy Simulations, AIAA-95-0356, 1995.
[30] C.C. Nelson, S. Menon, Unsteady Simulations of Compressible Spatial Mixing Layers, AIAA - 98 - 0786, 1998.
[31] C. Fureby, N. Alin, N. Wikstrom, S. Menon, N. Svanstedt, L. Persson, On Large Eddy Simulation of High Reynolds Number Wall Bounded Flows, AIAA Journal, Vol. 42, No. 3, 2004, pp. 457-469.
[32] S. James, J. Zhu, M. Anand, Large-Eddy Simulations as a Design Tool for Gas Turbine Combustion Systems. AIAA Journal, Vol. 44, No. 4, 2006, pp. 674-686.
[33] S. Kirpekar, D. Bogy, A Benchmark for the Flow across a Square Cylinder using Commercial CFD Codes, APS Division of Fluid Dynamics 58th Annual Meeting, November 2005, Chicago, IL.
[34]
[35] X1. Author, Title of the Paper, International Journal of Science and Technology, Vol.X, No.X, 200X, pp. XXX-XXX.
[36] X2. Author, *Title of the Book*, Publishing House, 200X.